Valley edge states with opposite chirality in temperature dependent acoustic media

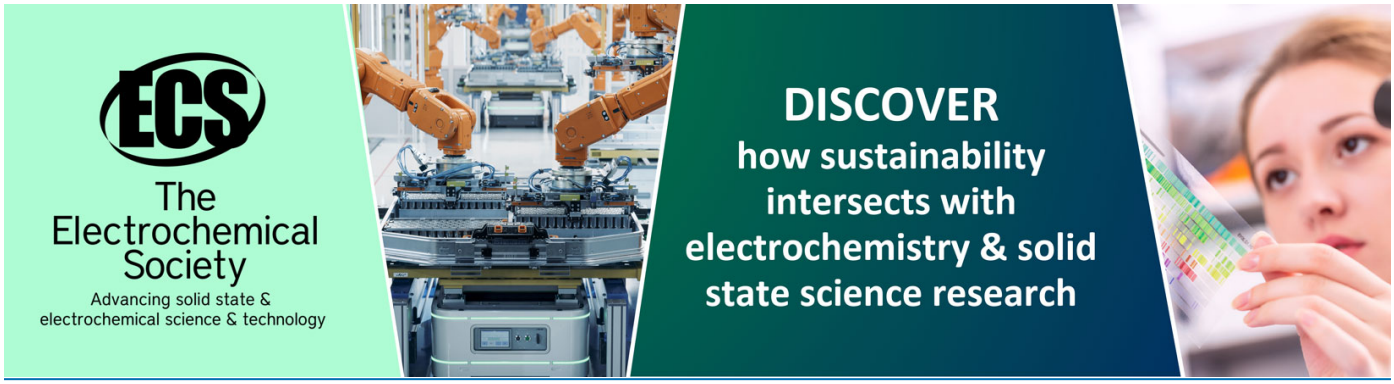

OPEN ACCESS
IOP Publishing
Journal of Physics D: Applied Physics
J. Phys. D: Appl. Phys. **57** (2024) 345303 (11pp)
https://doi.org/10.1088/1361-6463/ad4f9a

Valley edge states with opposite chirality in temperature dependent acoustic media

Muhammad Gulzari[1,2,*], Quan Zhang[3], Eoin King[1], Lihong Tong[4] and S K Lai[5]

[1] Department of Mechanical Engineering, School of Engineering, University of Galway, University Road, Galway H91 TK33, Ireland
[2] Construct Innovate, University of Galway, University Road, Galway H91 TK33, Ireland
[3] School of Mathematical and Statistical Sciences, University of Galway, University Road, Galway H91 TK33, Ireland
[4] Institute of Geotechnical Engineering, School of Civil Engineering and Architecture, East China Jiaotong University, Nanchang 330013, Jiangxi, People's Republic of China
[5] Department of Civil and Environmental Engineering, The Hong Kong Polytechnic University, Kowloon, Hong Kong Special Administrative Region of China, People's Republic of China

E-mail: m.muhammad@universityofgalway.ie

Received 18 March 2024, revised 25 April 2024
Accepted for publication 23 May 2024
Published 31 May 2024

Abstract

The valley degree of freedom in phononic crystals and metamaterials holds immense promise for manipulating acoustic and elastic waves. However, the impact of acoustic medium properties on valley edge state frequencies and their robustness to one-way propagation in valley topological phononic crystals remains unexplored. While significant attention has been devoted to scatterer design embedded in honeycomb lattices within acoustic and elastic media to achieve valley edge states and topologically protected nontrivial bandgaps, the influence of variations in acoustic medium properties, such as wave velocity and density affected by environmental temperature, has been overlooked. In this study, we investigate the effect of valley edge states and topological phases exhibited by topological phononic lattices in a temperature-dependent acoustic medium. We observe that a decrease in wave velocity and density, influenced by changing environmental temperature, shifts the topological valley edge states to lower frequencies. Therefore, alongside phononic lattice design, it is crucial to consider the impact of acoustic medium properties on the practical application of acoustic topological insulators. This issue becomes particularly significant when a topological phononic crystal is placed in a wave medium that transitions from incompressible to compressible, where wave velocity and density are no longer constant. Our findings offer a novel perspective on investigating topological insulators in variable acoustic media affected by changing thermodynamic and fluid properties.

Keywords: acoustic topological insulator, phononic crystals, valley edge states, interface mode, nontrivial bandgap

* Author to whom any correspondence should be addressed.

1. Introduction

Topological acoustics has emerged as a rapid and fascinating branch of topological physics followed by groundbreaking discoveries in solid-state physics that revealed the existence of topological states of matter [1–8]. Since then, researchers have tried to create acoustic analogue of selected mechanisms and they are majorly classified into three categories: acoustic quantum Hall effect (QHE), quantum spin Hall effect (QSHE), and quantum valley Hall effect (QVHE). The acoustic QHE is designed by breaking the time-reversal symmetry [9]. The acoustic QSHE with fourfold Dirac degeneracy is related to high symmetry at the centre point of the first irreducible Brillouin zone (FIBZ), i.e. Γ point. By manipulating the lattice symmetry, the band inversion triggered by topological phase transition with degenerate hybridized modes carrying opposite spins at the topological nontrivial bandgap bounding edges can be observed [10–12]. The acoustic QVHE with single Dirac cone degeneracy at the $K(K')$ point of FIBZ can be achieved by breaking the space-inversion symmetry (SIS) of the honeycomb lattice structure [12–14]. This results in a pair of separated valley edge states with opposite chirality at the bounding edges of the topological bandgap [15, 16]. Similar to the prior two mechanisms, the topological valley edge states can robustly propagate along the interface of two domains with opposite topological valley phases [17, 18].

The spin magnetic moment of the electron and the vortex pseudospin in phononic crystals are two intriguing phenomena that share some similarities. Both involve a form of angular momentum associated with the particles or excitations in the system. However, they arise in distinct physical contexts and have different underlying mechanisms. The spin magnetic moment of the electron is a fundamental property of electrons in quantum mechanics [19]. It arises from their intrinsic spin angular momentum, which is a quantum mechanical property that gives rise to a magnetic moment even in the absence of orbital motion. This magnetic moment interacts with external magnetic fields, leading to phenomena such as the Zeeman effect [20] and the Stern–Gerlach experiment [21].

On the other hand, vortex pseudospin in phononic crystals [15] is a concept that emerges in the study of wave propagation in structured media such as phononic crystals. In certain types of phononic crystals with topological properties, wave modes can exhibit a pseudospin degree of freedom analogous to the spin of electrons. This pseudospin can be associated with the chirality or rotational properties of the wave modes, leading to phenomena such as topologically protected edge states and unconventional wave transport [7, 22].

The field of acoustic topological QVHE is experiencing rapid advancement due to its adaptability and variety, offering a new avenue for manipulating the propagation of acoustic waves [23–27]. Numerous captivating subjects related to valley properties have been explored, such as topological one-way edge states [2, 3, 28], acoustic topological insulators [29, 30], acoustic topological rainbow trapping [31, 32] and topological valley transport [14, 33, 34]. Typically, achieving the valley edge states involve conveniently adjusting the phononic crystal (PnC) scatterers' orientation such that to lower the symmetry from C_{3v} to C_3, so called breaking SIS. While number of studies have investigated different honeycomb lattice designs with broken SIS characteristic, to the best of our knowledge, no study has considered the effect of acoustic wave medium properties such as varying acoustic wave speed (influenced by environmental temperature and pressure) and density on topologically protected valley edge state eigenfrequencies and robustness of acoustic wave propagation at the interface. Beside other reported works that began with fascinating topological PnC design with SIS, we considered a relatively simple structure that can support valley edge states in an acoustic medium with varying wave speed and densities. The proposed topological scatterer also supports structural reconfigurability [35] and detailed discussion on this structural attribute is outside the scope of this study.

The motivation for this study arises from a curiosity about how variations in the acoustic properties of wave media influence the valley edge states and the transportation of acoustic waves at the protected interface. In this paper we have considered acoustic wave propagating media whose properties are varying with working environmental temperature and atmospheric pressure. Since experimental data on acoustic variations for methyl nonafluorobutyl ether (MNE) and ethyl nonafluorobutyl ether (ENE) are available [36], we have majorly focused on studying topological valley edge states and topological phases in MNE and ENE media. However, the study implication is not limited to MNE and ENE and can be applied to other acoustic wave medium whose acoustic properties are changing under the influence of external stimuli. This includes the application of acoustic topological insulators in incompressible (constant density) and compressible (varying density) fluid media. MNE and ENE are sustainable biochemical solvents with a wide range of applications in cosmetic, biochemicals, and pharmaceutical products. Recently, Muhammad [37] discovered Fano resonance phenomena and proposed a new application of PnC as a bio-chemical sensor to detect the acoustic variations in MNE and ENE fluids.

In this study, we propose a two-dimensional PnC hexagonal lattice with C_{3v} symmetric scatterer that is comprised of three rectangular steel rods. The SIS in the proposed structure can be broken by rotating the three-legged rectangular steel rods inside the hexagonal lattice and topological valley edge states with opposite chirality can be realised. The presence of two separate chiral valley pseudospins, each with a distinct nonzero Chern number [14, 15], resulted in the band inversion and subsequently triggered a topological phase transition. The three rods are placed at an angle of 120 degrees inside the hexagonal lattice and by changing the orientation of the PnC scatterer, we can increase the bandwidth of the topological bandgap. The PnC scatterer is placed in the MNE and ENE media and the effect of varying acoustic properties i.e. sound speed influenced by changing temperature [36] on the topological nontrivial bandgap and valley edge states is investigated. The effect of MNE and ENE temperature on Dirac degeneracy frequency is discussed. By varying the acoustic properties of MNE and ENE, we have reported robust acoustic wave propagation at the straight and zigzag interfaces without

changing the geometric parameters of the scatterer. The study contributes by providing new findings on understanding the impact of acoustic medium properties on valley topological phases and interface state frequencies. It is expected that our findings will open a new avenue for the application of acoustic topological insulators in compressible and incompressible fluid media where external stimuli (temperature and pressure) influence acoustic medium properties.

The remaining paper is organized as follows: section 2 discusses the methodology and valley edge states with vortex features in a single unit cell PnC honeycomb lattice. The valley edge states with opposite chirality influenced by breaking SIS in the supercell lattice structure is explained in section 3. The acoustic wave propagation at the straight and zigzag interfaces are demonstrated in section 4. Finally, the study conclusion and outlook are given in section 5.

2. Acoustic valley edge states and opposite chirality

The PnC hexagonal unit cell structure is shown in figure 1(a). The unit cell structure consists of three-legged rectangular steel rods (as scatterer) placed 120 degrees apart inside an acoustic media. The acoustic media are comprised of MNE and ENE fluids. The central region enveloped by the rectangular steel rods is a regular triangle. The topological acoustic valley edge states in an air medium with a similar structure were recently studied by Xi *et al* [35]. We utilized this structure to investigate the acoustic valley edge states and topologically protected interface mode propagation in the MNE and ENE media subjected to varying temperatures. The steel scatterer has material properties as follows: mass density $\rho = 7850\ \mathrm{kg\ m^{-3}}$, Young's modulus $E = 210$ GPa, and Poisson ratio $\nu = 0.33$. The acoustic properties of MNE and ENE fluids under varying temperatures are given in table 1 [36]. The lattice constant of the hexagonal lattice is $a = 40$ mm with geometric parameters of the rectangular steel rods as follows: width $w = 9$ mm, height $h = 13$ mm. The side length of the hexagon is $a/2$. All three rectangular rods can rotate around their centre with an angle θ to break the SIS of the unit cell structure. The matched mirror symmetry between the hexagonal lattice and scatterer enables the structure to exhibit a single Dirac point at the high symmetry K and K' points on the FIBZ. Due to high symmetry in the proposed hexagonal lattice, Dirac degeneracy can be inevitably produced in the FIBZ. Due to inherent property of the proposed lattice structure, by changing the angle θ, the mirror symmetry of C_{3v} can be broken and transformed to C_3 symmetry. This will result in lifting Dirac cone degeneracy and opening of topologically protected nontrivial bandgap bounded by the distinct valley edge states and topological phases.

The present study is conducted by using finite element code COMSOL Multiphysics v6.2. We used the pressure acoustics physics to model MNE and ENE media. The three-legged steel scatterers are modelled using solid mechanics physics. The Floquet Bloch periodicity condition is applied on all six edges of the hexagonal lattice to make the unit cell structure infinitely periodic in the x and y directions. The COMSOL Multiphysics eigenfrequency study is used to solve the wave dispersion relation and analyse the topological phases with opposite chirality. We used the frequency domain study to demonstrate acoustic wave propagation in topologically protected supercell lattices with straight and zigzag interfaces.

For the proposed lattice structure, when the angle of rotation θ is 30 degrees, the Dirac cone degeneracy is observed, see figure 1(b). By rotating the rectangular steel rods ± 30 degrees i.e. $\theta = 0°$ or $\theta = 60°$, the SIS can be broken as a result Dirac cone degeneracy that was initially observed for $\theta = 30°$can be lifted and a complete topologically protected nontrivial bandgap with distinct Chern number and topological phases can be observed. Figure 1(c) shows the simulated acoustic energy and intensity fields for two different valley edge states labelled as p^- and q^+ on the first two acoustic bands when $\theta = 0°$ (Type I) and $\theta = 60°$ (Type II). From the acoustic energy and intensity fields for p^- and q^+ modes, one can clearly observe the typical vortex profiles with clockwise and counterclockwise acoustic energy flow, so-called valley pseudospin effect around the honeycomb lattice centre, respectively. In addition, the six vertices of the hexagonal lattice are labelled with p and q alternately, see figure 1(a) red dashed line. The three p and central triangular regions show clockwise acoustic energy flow for p^- mode, see blue arrows in figure 1(d). Likewise, the acoustic pressure intensity profile for q^+ mode shows the counterclockwise acoustic energy flow for the other three hexagonal vertices labelled with q and central triangular region, see black arrows in figure 1(d).

To reveal the topological phase transition of the two-dimensional hexagonal lattice, valley Hall transition in the FIBZ is studied by determining the eigenfrequencies and eigenmodes of the valley edge states for different rotation angle θ. Since each rectangular steel rod is separated 120 degrees apart, we cannot rotate the three legs of the scatterer more than 60 degrees to get different topologies. Therefore, the valley edge state eigenfrequencies and eigenmodes are determined in the range of $-60° \leqslant \theta \leqslant 60°$ for MNE and ENE acoustic media separately. Figure 2 shows the band transition with Dirac degeneracy opening, closing, and reopening of the nontrivial topological bandgap for MNE and ENE fluids at room temperature of 25 °C. When $\theta = 30°$, Dirac degeneracy is observed at 8.075 kHz (MNE) and 8.372 kHz (ENE) at K point of FIBZ. By varying the angle θ above or below 30°, Dirac degeneracy is lifted by breaking SIS and a topological nontrivial bandgap emerges. The topological valley phases at the bounding edges of the bandgap showed that band inversion has occurred at $\theta = 30°$. This can be observed from clockwise (p^- mode) and counterclockwise (q^+ mode) acoustic energy flow/mode polarization in the hexagonal lattice.

Furthermore, the valley edge eigenfrequencies are determined for both MNE and ENE under varying environmental temperatures ranging from 10 °C–40 °C, see table 1. The temperature variation altered the density and sound speed of

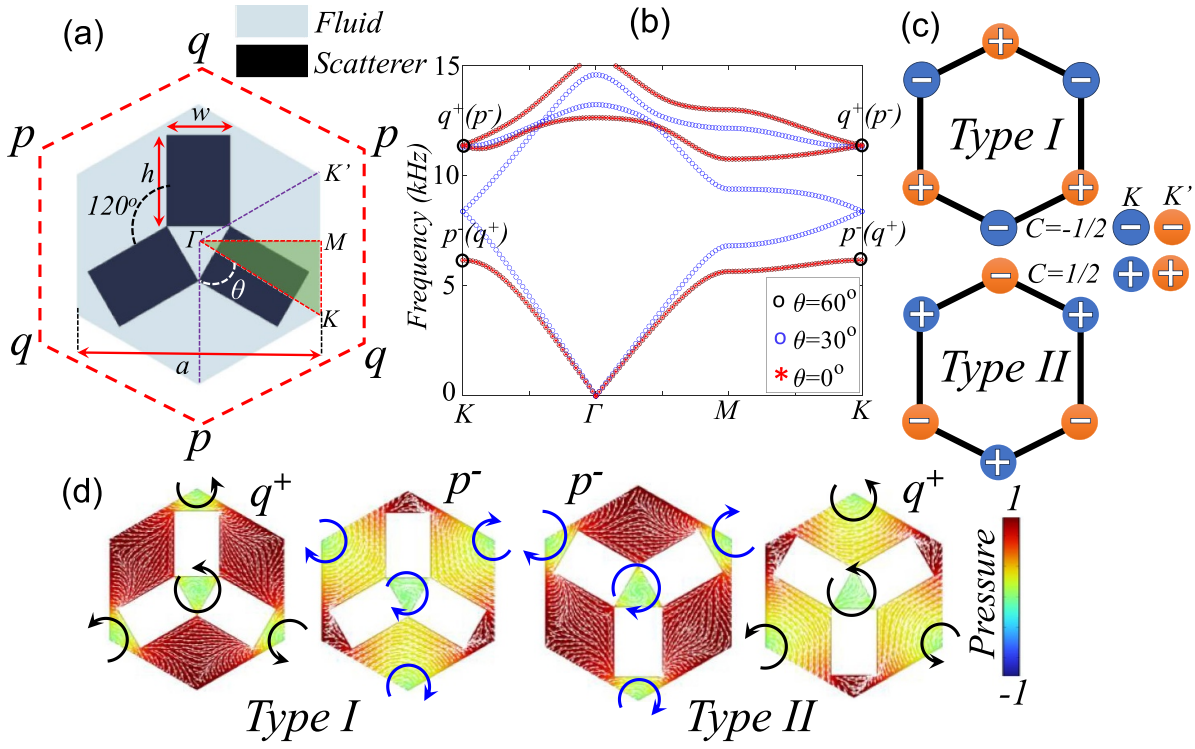

Figure 1. (a) Schematic of the PnC honeycomb lattice formed by embedding three-legged steel scatterers inside an acoustic media comprising of MNE and ENE fluids. (b) Dispersion plot of PnC lattice at rotation angle of $\theta = 0°, 30°, 60°$ with Dirac degeneracy at $\theta = 30°$. The SIS can be achieved by changing the rotation angle $60° \leqslant \theta \leqslant 0°$. (c) The valley Chern numbers that characterize the distinct valley-dependent behaviours. (d) Valley pseudospin with opposite chirality (clockwise and counterclockwise acoustic energy flow) observed at the bounding edge of the nontrivial topological bandgap when $\theta = 0°$ and $\theta = 60°$. The white arrows show direction of in-plane acoustic velocity in spatial frame.

Table 1. Acoustic properties of MNE and ENE with varying temperatures (10 °C–40°C) at atmospheric pressure of 1 atm. The data are obtained from Piñeiro *et al* [36].

	MNE		ENE	
Temperature (°C)	Density (kg m^{-3})	Wave speed (m s^{-1})	Density (kg m^{-3})	Wave speed (m s^{-1})
10	1554	650.5	1455	669.9
15	1540	634	1445	650.2
20	1527	617	1438	638.2
25	1515	600.2	1433	622.6
30	1501	584	1415	607.4
35	1488	568	1398	592.3
40	1474	551.7	1383	575.5

MNE and ENE, as a result eigenfrequency of valley edge states changed. However, eigenmodes are not affected by the acoustic property of the wave medium as it is influenced by scatterer geometry rather than acoustic medium property, therefore identical valley edge states can be presumed for both MNE and ENE with changing temperature. The valley edge states with interchangeable eigenmode polarization i.e. clockwise p^- mode and counterclockwise q^+ mode with acoustic energy flow (white arrows) can be observed in figure 3(a). For instance, when $\theta = \pm 30°$, a Dirac cone degeneracy can be observed at 8.075 kHz (MNE) and 8.372 kHz (ENE). The effect of temperature on the Dirac cone degeneracy frequency for MNE and ENE at $\theta = \pm 30°$ is shown in figures 3(b) and (c).

When $\theta = \pm 60°$, the lower bounding edge of the topological bandgap has clockwise polarization/ acoustic energy flow i.e. p^- mode, and the upper bounding edge has counterclockwise polarization/acoustic energy flow i.e. q^+ mode as shown in figure 3(a). With decreasing rotation angle θ, the topological bandgap becomes narrower until $\theta = -30°$ where Dirac degeneracy or topological bandgap closing is observed. Such band inversion usually occurs across a nontrivial topological bandgap that is bounded by the trivial and nontrivial bounding edges with opposite chirality. When θ is further increased beyond $\theta = -30°$, the topological nontrivial bandgap opens again, however, opposite chirality and valley pseudospin behaviour are observed. Even though $\theta = 0°$ and $\theta = -60°$ have identical eigenfrequencies i.e. wave dispersion

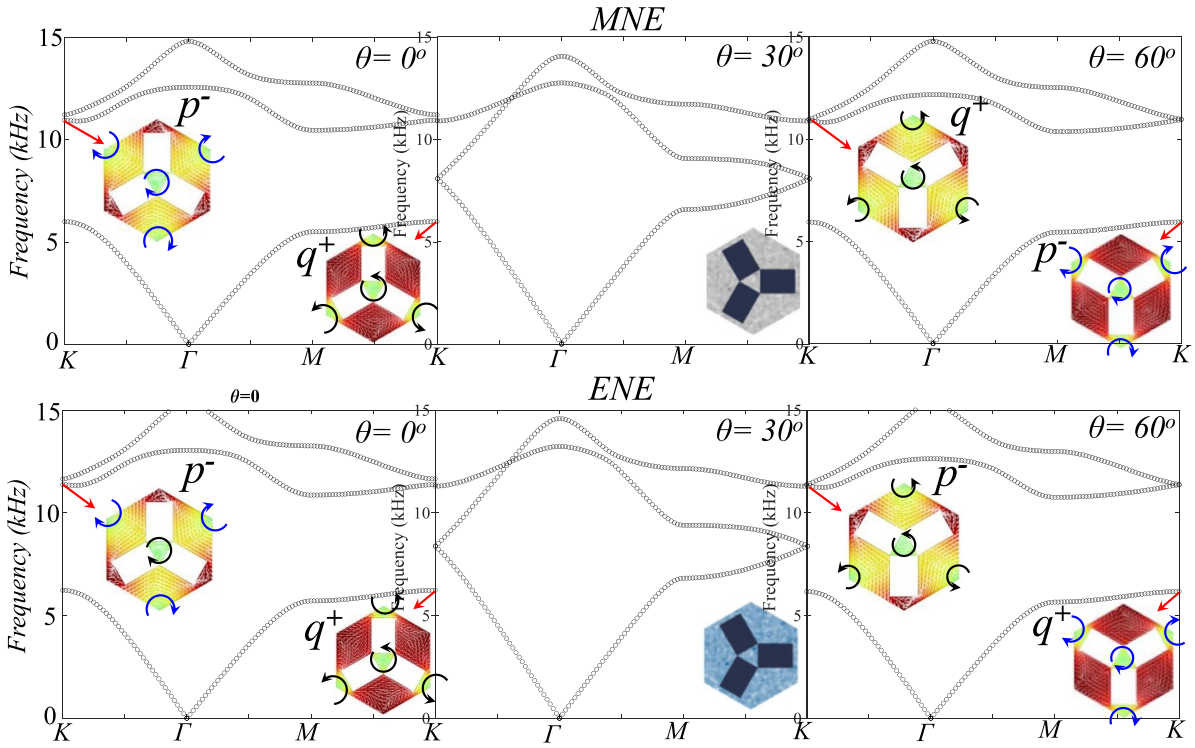

Figure 2. Band structure of PnC scatterers in MNE and ENE acoustic media at temperature of 25 °C for $\theta = 0°, 30°, 60°$ across the boundary of FIBZ. Dirac degeneracy with band inversion at K point for $\theta = 30°$ can be observed. An opening of a complete topologically protected nontrivial bandgap is achieved for $\theta = 0°, 60°$. The acoustic energy flow direction (black and blue arrows) and eigenmode polarization (clockwise p^- and counterclockwise q^+ eigenmodes) are shown in the figure inset.

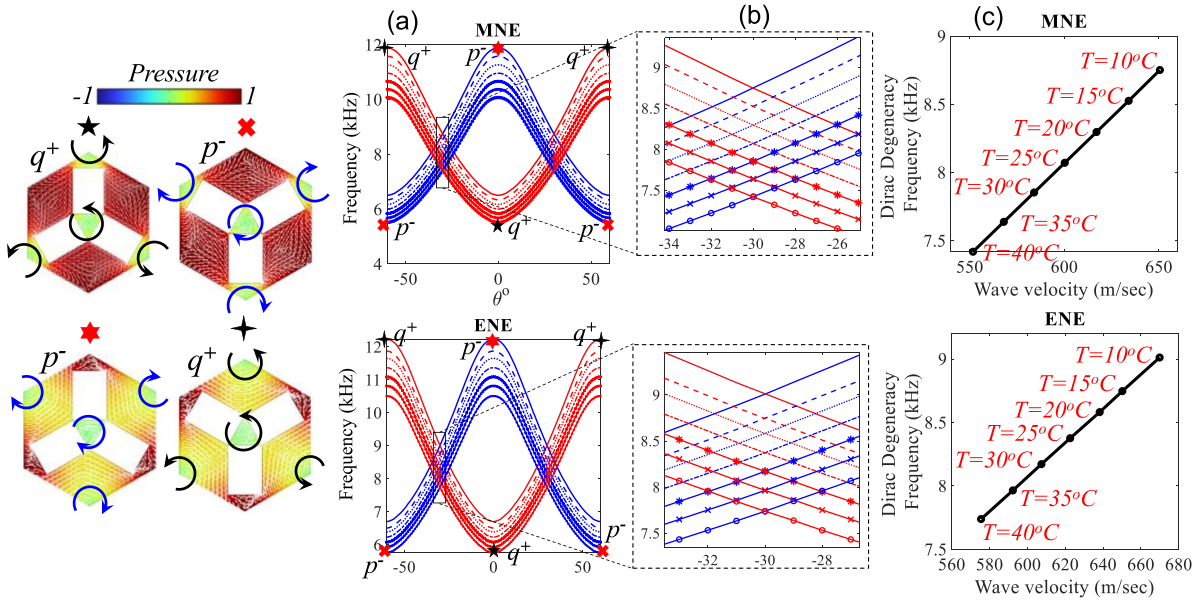

Figure 3. (a) Topological phase diagram exhibiting topological phase transition with changing rotation angle θ ranging from $-60°$ to $60°$ for acoustic wave propagating in MNE and ENE media with changing temperature. The eigenmodes at the left side show the specific vortex feature of the valley edge states at the bounding edge of the nontrivial topological bandgap when $\theta = \pm 60°$ and $\theta = 0°$. (b) The zoomed Dirac degeneracy frequency with band inversion for MNE and ENE at different temperatures. (c) The Dirac degeneracy frequency with changing temperature for MNE and ENE acoustic wave media.

curves, they show opposite chirality in their eigenmodes. For $-30° \leqslant \theta \leqslant 0°$ range, the lower bounding edge of the topologically protected nontrivial bandgap has counterclockwise polarization i.e.q^+ mode, see figure 3(a). While the upper bounding edge has clockwise polarization i.e. p^- mode, which is opposite to valley edge state polarisation behaviour observed in$-60° \leqslant \theta \leqslant -30°$ range. Identical behaviour with interchangeable valley edge state polarization is observed for

the other second half part of the Dirac plot where opening, closing, and reopening of the nontrivial topological bandgap is observed. This showed that before and after $\theta = \pm 30^\circ$ when Dirac degeneracy is lifted, nontrivial topological bandgap with exchange in valley edge state polarization has occurred. These Dirac plots for MNE and ENE also show that with variation in acoustic properties of wave media, the eigenfrequency of valley edge states has changed while eigenmodes remained the same. An increase in wave velocity and/or acoustic wave medium density shifted the valley edge states and Dirac degeneracy to a lower frequency.

By applying $\mathbf{k}\cdot\mathbf{p}$ perturbation method [38, 39], the Dirac degeneracy and the so-called valley Hall phase transition around K point of FIBZ can be described by θ-dependent continuum Hamiltonian $H_K(\delta\mathbf{k}) = \upsilon_D(\delta k_x\sigma_x + \delta k_y\sigma_y) + m\upsilon_D^2\sigma_z$ where υ_D is Dirac velocity, $\delta\mathbf{k}$ is the moment derivation of $\mathbf{k}-\mathbf{k}_K$ from the valley centre K, and $\sigma_i(i = x,y,z)$ are Pauli matrices that operate on the vortex pseudospins. The effective mass is $m = (\omega_{q+} - \omega_{p-})/2\upsilon_D^2$. The Hamiltonian depends upon the rotation angle θ through the bounding edge frequencies ω_{q+} and ω_{p-} in the effective mass term. The Berry curvature can be derived from this Hamiltonian using the expression $\Omega(\delta\mathbf{k}) = \frac{m\upsilon_D\left(|\delta\mathbf{k}|^2+m^2\upsilon_D^2\right)^{-\frac{3}{2}}}{2}$. Further integration of the Berry curvature will lead us to an expression $C_K = \frac{\gamma}{2} = \frac{1}{2\pi}\int\Omega(\delta\mathbf{k})\,d^2\delta\mathbf{k}$ where C_K is Chern number and γ is Berry phase. The theoretical valley Chern number for K and K'valleys can be calculated using $C_K = \frac{\mathrm{sgn}(m)}{2}$ and $C_{K'} = -\frac{\mathrm{sgn}(m)}{2}$ respectively [38].

3. Valley edge states in supercell structures

Following the discussion on the valley edge states and topological phases, we categorise the proposed hexagonal lattice into Type I ($\theta = 0^\circ$) and Type II ($\theta = 60^\circ$) lattices. For Type I hexagonal lattice with $\theta < 30^\circ$, the theoretical valley Chern number at K and K' points are $-\frac{1}{2}$ and $+\frac{1}{2}$ respectively. While for Type II hexagonal lattice with $\theta > 30^\circ$, these are opposite as schematically shown in figure 1(c). These distinct features offer an opportunity to obtain valley edge states at the interface of Type I and Type II hexagonal lattices. Prior to revealing the topologically protected interface states at the interface of Type I & II lattices, band structure studies of 12 Type I and 12 Type II hexagonal lattices are carried out to demonstrate valley edge states in the supercell structure. As shown in figure 4, localization of acoustic energy at the interface of Type I and Type II lattices corresponding to wavenumber k^{n+} (k^{p-})with a decaying energy field away from the interface is observed. The superscript p and n show positive and negative wavenumbers while the $-ve$ and $+ve$ superscript symbols show the backward and forward acoustic wave propagation. Even though wavenumber k^{n+} (k^{p-}) is symmetric with reference to the FIBZ centre, they have opposite polarization of acoustic energy flow. The k^{n+} band is shown with blue and k^{p-} band is depicted with red dotted lines. Their distinct clockwise and counterclockwise edge mode polarization at the interface with the direction of acoustic energy flow (white arrows) is shown in the figure inset. The acoustic wave energy at wavenumber k^{n+} features forward clockwise and counterclockwise pseudospins above and below the interface, respectively. While the acoustic wave energy at the k^{p-} wavenumber has an opposite pseudospin direction with backward acoustic energy propagation. For both wavenumbers k^{n+} (k^{p-}) the evolution of pseudospin acoustic pressure field from 0 to 2π is shown at the bottom of figure 4.

The band structure of supercell lattices shown in figure 4 is for MNE and ENE at operating temperature of $10\,^\circ C$. Next, we changed the temperature for both MNE and ENE within the given temperature range, see table 1, and depicted the interface mode band in a rainbow colour spectrum, see figure 5. For convenience, the k^{n+} (k^{p-}) wavenumber is shown with the same colours, hence readers are suggested to keep the discussion on figure 4 into consideration when analysing figure 5. Reminiscent of the findings in figure 3, a decrease in interface mode eigenfrequencies is observed with increasing temperature of MNE and ENE media. The localization of acoustic wave energy at the interface of Type I and Type II lattices is shown in the inset of figure 5.

4. Acoustic wave propagation at interface

In this section we will explain the acoustic wave propagation at the interface of Type I and Type II lattices by arranging the supercell structure in such a way to form straight and zigzag interfaces. A circular region (loudspeaker symbol) is used to induce acoustic plane wave and excite the valley edge states at the interface of topologically distinct PnCs for a frequency range covering the topological bandgap. To avoid incident acoustic wave back reflection from domain boundaries that may obscure the results, the entire system is surrounded by a perfectly matched layer. By using the frequency domain study in COMSOL Multiphysics, a wide range of frequencies are swept to visualize the acoustic wave propagation at the interface of Type I and Type II PnC lattices. For a straight interface formed by the Type II PnC lattice at the top and the Type I PnC lattice at the bottom, robust acoustic wave propagation can be observed in figure 6(a). The interface of lattice structures is shown with the red line. We used two probes to measure the acoustic pressure intensity at the interface and a point away from the interface, see microphone symbols in figure 6(a). Inside the bandgap region of the supercell lattice (see figures 4 and 5), robust acoustic wave propagation at the interface while decaying acoustic pressure intensity fields away from the interface are obtained. We calculated the frequency response spectra at different temperatures for MNE, using data given in table 1. The blue dash-dot line shows the decaying acoustic energy for the point probe away from the interface. While the black solid line shows the robust propagation of acoustic energy along the interface of Type I and Type II PnC lattices. The influence of MNE temperature (that alters acoustic wave velocity and density) on the frequency response spectra is shown in figures 6(b)–(i). Like figures 3 and 5, a

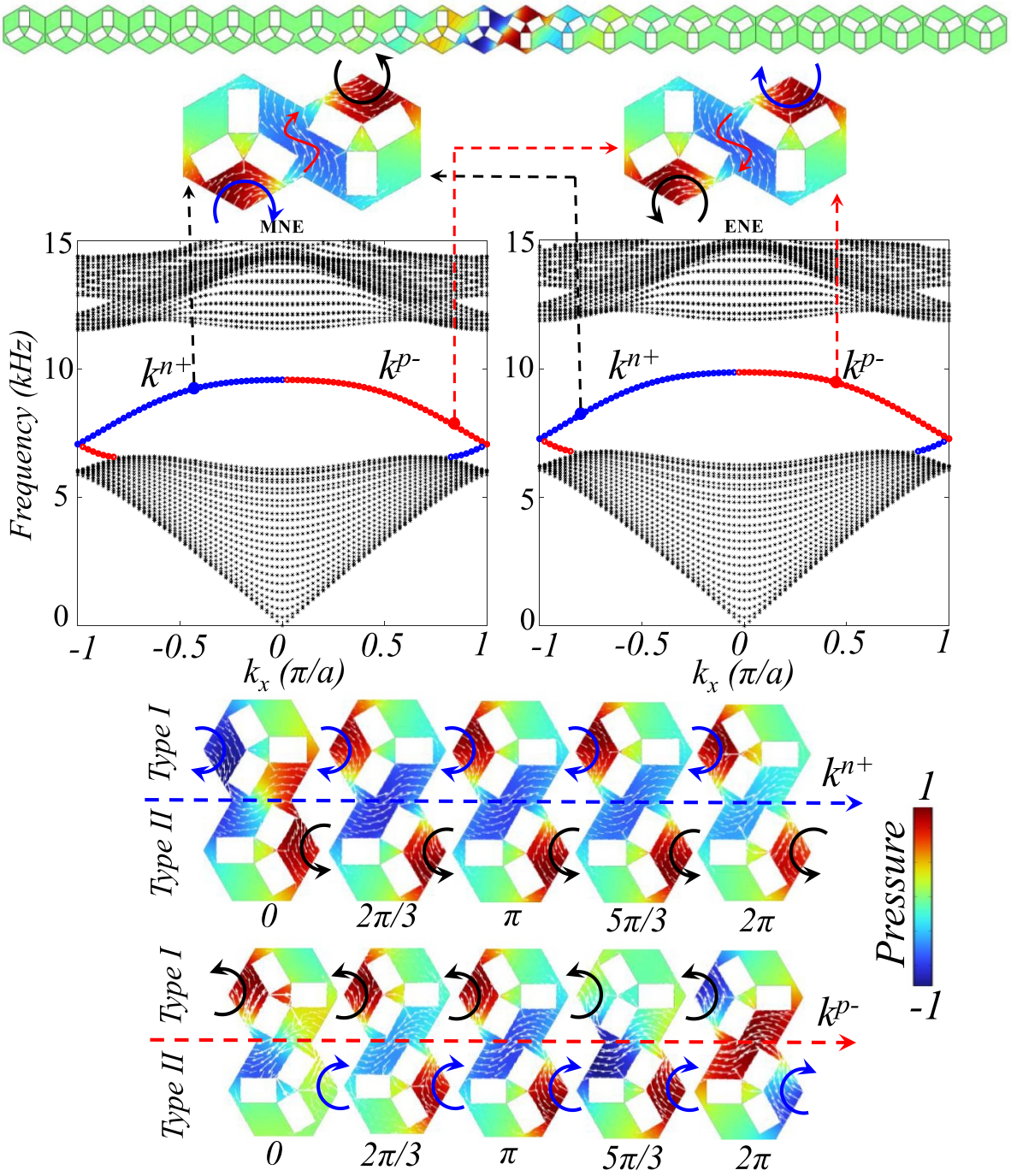

Figure 4. Band structure of supercell lattice structure consisting of 12 Type I and 12 Type II PnC lattices. The localization of acoustic energy at the interface of Type I and Type II lattices is shown at the top. Such interface mode can be observed for eigenfrequencies positioned at the k^{n+} and k^{p-} wavenumbers. The specific vortex feature of valley edge states at different values of k^{n+} and k^{p-} wavenumbers are shown. A forward acoustic wave energy flow at k^{n+} and backward acoustic wave energy flow at k^{p-} wavenumbers can be observed. The bulk acoustic modes are depicted with black asterisks.

decrease in valley edge state frequencies with increasing temperature for MNE is observed. This deduced that a decrease in sound speed in MNE media shifts the interface mode frequencies to a lower region.

Next, we arranged the Type I and Type II PnC lattice in a way to mimic the zigzag interface, see figure 7(a). The acoustic wave is excited in the ENE media and frequency response spectra are calculated. The zigzag interface further demonstrates the robustness of topologically protected valley edge states at the bends and sharp corners. Figures 7(b)–(i) shows the frequency response spectra for ENE with varying temperatures in the PnC lattice structure with a zigzag interface.

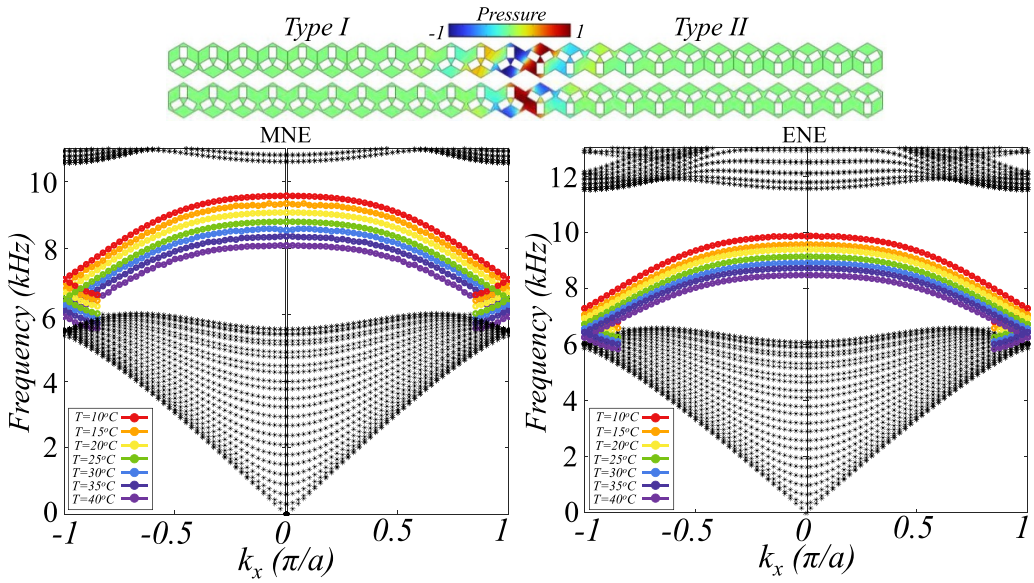

Figure 5. Band structure of PnC supercell lattices in the MNE and ENE acoustic media subject to varying temperatures. The variation in interface mode frequencies at k^{n+} and k^{p-} wavenumbers with changing temperature can be observed. Any eigenfrequency lying inside the topologically nontrivial bandgap region exhibits interface mode, as shown in the figure top.

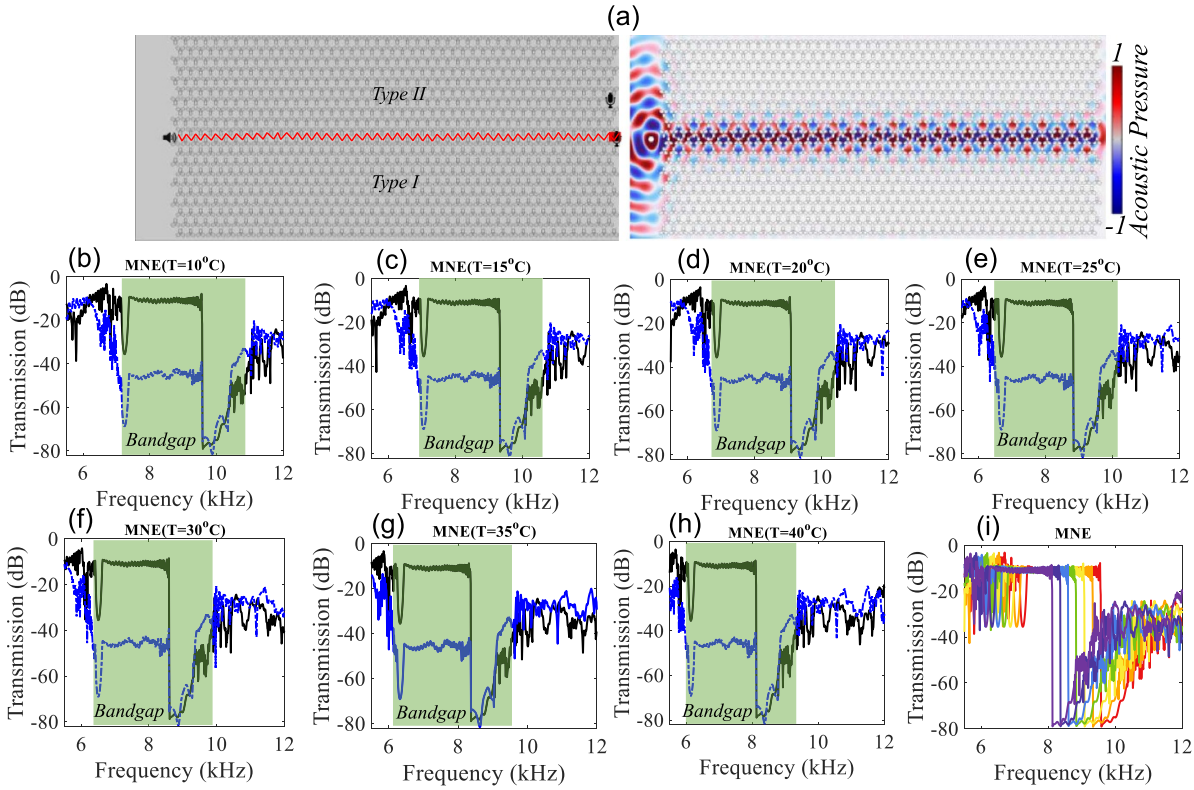

Figure 6. (a) A straight interface formed by the arrangement of Type I and Type II PnC lattices. The robust acoustic wave propagation at the straight interface can be observed. The excitation source (speaker symbol) and probe points (microphone symbol) are shown. (b)–(h) For MNE subject to varying temperatures (10 °C−40 °C), the frequency response spectra are obtained using two-point probes at the interface (solid black line) and a random point away from the interface (dashed blue line). The robustly propagating acoustic wave pressure at the interface (solid black line) and decaying acoustic wave energy inside the bandgap region (dashed blue line) can be observed. The bandgap region is highlighted in green. (i) The comparison of frequency response spectra with changing temperature at the interface probe.

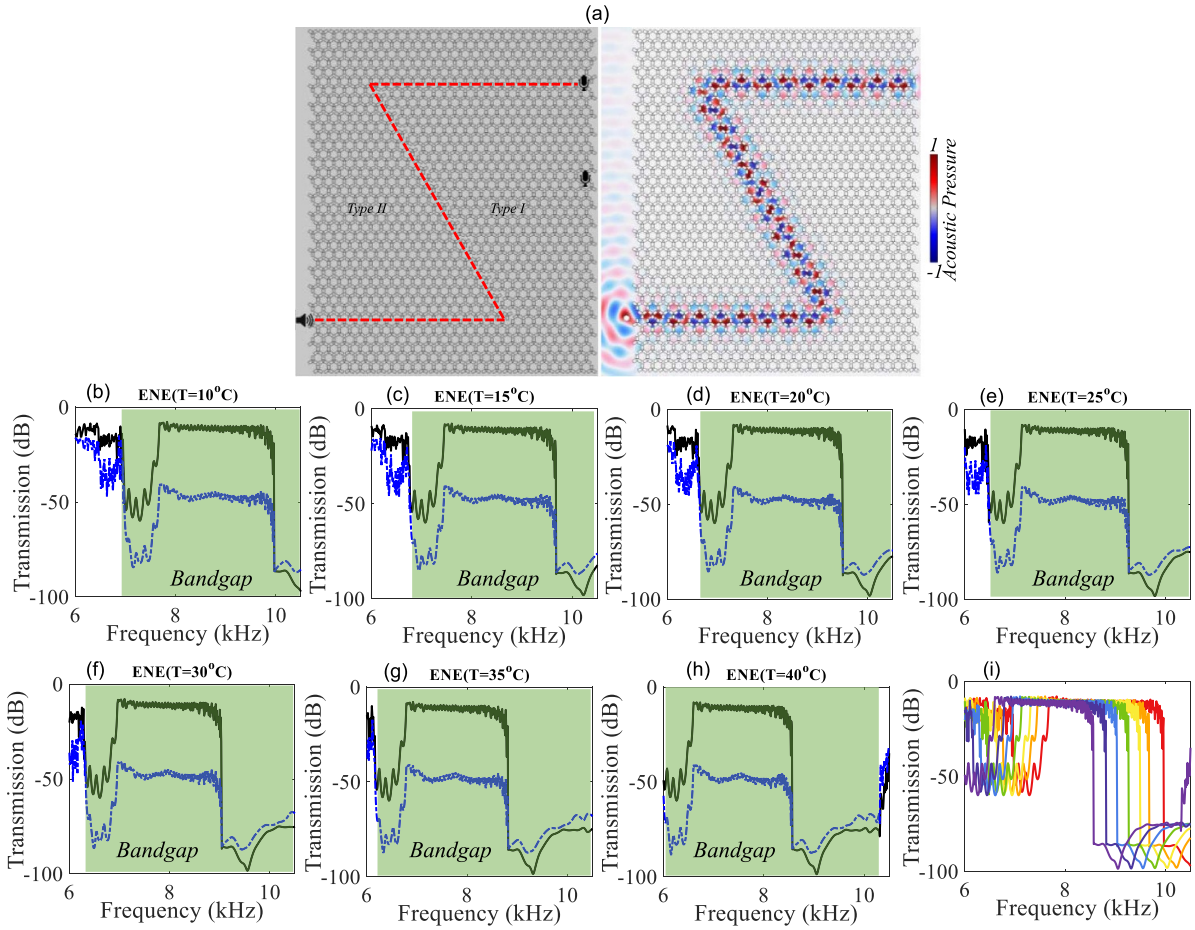

Figure 7. (a) A zigzag interface formed by arrangement of Type I and Type II PnC lattices. The robust acoustic wave propagation at the zigzag interface can be observed. The excitation source (speaker symbol) and probe points (microphone symbol) are shown. (b)–(h) For ENE subject to varying temperatures (10 °C−40 °C), the frequency response spectra are obtained using two-point probes at the interface (solid black line) and a random point away from the interface (dashed blue line). The robustly propagating acoustic wave pressure at the interface (solid black line) and decaying acoustic wave energy inside the bandgap region (dashed blue line) can be observed. The bandgap region is highlighted in green. (i) The comparison of frequency response spectra with changing temperature at the interface probe.

5. Conclusion and outlook

In this study, we explore acoustic valley edge states and topological phases within temperature-dependent MNE and ENE acoustic media. A phononic crystal periodic scatterer consisting of three-legged rectangular steel rods is arranged in a honeycomb lattice to investigate wave dispersion, Dirac degeneracy lifting, and pseudospin vortex features of valley edge modes along the bounding edges of the topologically nontrivial bandgap. Experimental data obtained from literature indicate that variations in the working temperature of MNE and ENE result in reduced wave speed and density of the acoustic media. By manipulating the temperature of MNE and ENE acoustic media, we analyse the effect of changing acoustic medium wave speed and density on valley edge state eigenfrequencies and eigenmodes. Our findings reveal that a decrease in the speed of sound in MNE and ENE media shifts the valley edge modes, including the Dirac degeneracy point, to a lower frequency region. We also investigate the pseudospin vortex features of valley edge modes with opposite chirality by constructing supercell structures with distinct topologies and conducting wave dispersion studies. Analysis of the supercell dispersion curves unveils forward and backward propagating acoustic bands at the interface of topologically distinct PnC lattices. We discuss the valley pseudospin with opposite vortex chirality for both unit cell structures and supercell lattices, elucidating their effect on changing acoustic medium properties influenced by temperature variation. Furthermore, we combine two types of topologically distinct unit cell structures to emulate straight and zigzag interfaces. Through frequency domain analysis, we examine the frequency response spectra for probe points at the interface and away from it. Our results demonstrate robust acoustic wave propagation at interface mode frequencies for straight and zigzag interfaces. This study represents a unique exploration of valley edge states in temperature-dependent acoustic media,

with significant implications for applications in acoustic topological insulators in thermodynamically controlled acoustic media.

Data availability statement

All necessary information required to reproduce the results are available in the main manuscript. If anyone wants to reproduce the results, all information is available. If the readership wish to ask for source files such as COMSOL Multiphysics and MATLAB scripts, they must write to corresponding author and upon request corresponding author will provide those files to particular readers. The data that support the findings of this study are available upon reasonable request from the authors.

Acknowledgments

This work was supported by Construct Innovate, Ireland's National Research Centre for Construction Technology and Innovation (Enterprise Ireland TC-2022-0033, Seed Fund Call CISFC1-23_002 and CISFC1-23_003).

Conflict of interest

The authors declare that they have no known competing financial interests or personal relationships that could have appeared to influence the work reported in this paper.

ORCID iDs

Muhammad Gulzari https://orcid.org/0000-0003-3492-0123
S K Lai https://orcid.org/0000-0003-2386-3821

References

[1] Yang Z, Gao F, Shi X, Lin X, Gao Z, Chong Y and Zhang B 2015 Topological acoustics *Phys. Rev. Lett.* **114** 114301
[2] Wang P, Lu L and Bertoldi K 2015 Topological phononic crystals with one-way elastic edge waves *Phys. Rev. Lett.* **115** 104302
[3] He C, Ni X, Ge H, Sun X-C, Chen Y-B, Lu M-H, Liu X-P and Chen Y-F 2016 Acoustic topological insulator and robust one-way sound transport *Nat. Phys.* **12** 1124
[4] Zhao D G, Xiao M, Ling C W, Chan C T and Fung K H 2018 Topological interface modes in local resonant acoustic systems *Phys. Rev.* B **98** 014110
[5] Ma G, Xiao M and Chan C T 2019 Topological phases in acoustic and mechanical systems *Nat. Rev. Phys.* **1** 281–94
[6] Zhang Z W, Tian Y, Cheng Y, Wei Q, Liu X and Christensen J 2018 Topological acoustic delay line *Phys. Rev. Appl.* **9** 034032
[7] Chen Z, Muhammad M, Wang X and Lim C W 2021 Low frequency topologically protected wave transport in sinusoidal lightweight acoustic metamaterials *J. Appl. Phys.* **130** 045108
[8] Muhammad, Ogun O and Kennedy J 2022 Inverse design of a topological phononic beam with interface modes *J. Phys. D: Appl. Phys.* **56** 015106
[9] Wen X, Qiu C, Qi Y, Ye L, Ke M, Zhang F and Liu Z 2019 Acoustic Landau quantization and quantum-Hall-like edge states *Nat. Phys.* **15** 352–6
[10] Chen J-H, Li Y, Yu C, Fu C and Hang Z H 2022 Realization of the quantum spin Hall effect using tunable acoustic metamaterials *Phys. Rev. Appl.* **18** 044055
[11] Kawada T, Kawaguchi M, Funato T, Kohno H and Hayashi M 2021 Acoustic spin Hall effect in strong spin-orbit metals *Sci. Adv.* **7** eabd9697
[12] Deng Y, Lu M and Jing Y 2019 A comparison study between acoustic topological states based on valley Hall and quantum spin Hall effects *J. Acoust. Soc. Am.* **146** 721–8
[13] Zhou W, Su Y, Muhammad, Chen W and Lim C W 2020 Voltage-controlled quantum valley Hall effect in dielectric membrane-type acoustic metamaterials *Int. J. Mech. Sci.* **172** 105368
[14] Wang Z *et al* 2021 Multichannel topological transport in an acoustic valley Hall insulator *Phys. Rev. Appl.* **15** 024019
[15] Tian Z, Shen C, Li J, Reit E, Bachman H, Socolar J E S, Cummer S A and Jun Huang T 2020 Dispersion tuning and route reconfiguration of acoustic waves in valley topological phononic crystals *Nat. Commun.* **11** 762
[16] Sun X-W, Tan M-T, Xu G-G, Cao Y, Wen X-D and Liu Z-J 2024 Sub-wavelength topological boundary states and rainbow trapping of local-resonance phononic crystal plate *J. Appl. Phys.* **57** 225302
[17] Gou X-H, Lai H-S, Sun X-C, Yu S-Y, Chen Y B, He C and Chen Y-F 2024 Observation of double-kink states in multivalley acoustic crystals *Phys. Rev.* B **109** 054109
[18] Li J, Deng C, Zhang K, Lu Q and Yang H 2023 Higher-order topological states in dual-band valley sonic crystals *Appl. Phys. Lett.* **123** 253101
[19] Levitt M H 2013 *Spin Dynamics: Basics of Nuclear Magnetic Resonance* (Wiley)
[20] Jiang C, Liu F, Cuadra J, Huang Z, Li K, Rasmita A, Srivastava A, Liu Z and Gao W-B 2017 Zeeman splitting via spin-valley-layer coupling in bilayer $MoTe_2$ *Nat. Commun.* **8** 802
[21] Wennerström H and Westlund P-O 2017 A quantum description of the Stern–Gerlach experiment *Entropy* **19** 186
[22] Muhammad, Zhou W and Lim C W 2019 Topological edge modeling and localization of protected interface modes in 1D phononic crystals for longitudinal and bending elastic waves *Int. J. Mech. Sci.* **159** 359–72
[23] Muhammad and Lim C W 2021 From photonic crystals to seismic metamaterials: a review via phononic crystals and acoustic metamaterials *Arch. Comput. Methods Eng.* **29** 1137–98
[24] Ni X *et al* 2023 Topological metamaterials *Chem. Rev.* **123** 7585–654
[25] Tsuruta K 2023 Acoustic metasurfaces and topological phononics for acoustic/elastic device design *Jpn. J. Appl. Phys.* **62** SJ0803
[26] Zhu W *et al* 2023 Topological phononic metamaterials *Rep. Prog. Phys.* **86** 106501
[27] Chen Y, Chen J-H, Wu F, Chen H and Zheng Z-H 2023 Topological edge states on the acoustic Mobius band *Results Phys.* **46** 106322
[28] Yuan W, Zhao J, Long Y, Ren J and Zhong Z 2021 Multi-branch valley-chiral edge states of antisymmetric plate wave in phononic crystal plates with double-sided symmetric pillars *Int. J. Mech. Sci.* **197** 106347
[29] Xia J-P, Jia D, Sun H-X, Yuan S-Q, Ge Y, Si Q-R and Liu X-J 2018 Programmable coding acoustic topological insulator *Adv. Mater.* **30** e1805002

[30] Xiong W, Gao P, Zhang Z, Yue Z, Zhang H, Cheng Y, Liu X and Christensen J 2021 Demultiplexing sound in stacked valley-Hall topological insulators *Phys. Rev.* B **104** 224108
[31] Fu C-M *et al* 2024 Defect-adjusted valley edge states and rainbow trapping of elastic waves in 2D topological phononic crystals *Phys. Status Solidi* **18** 2300334
[32] Tang X-L, Ma T-X and Wang Y-S 2023 Topological rainbow trapping and acoustic energy amplification in two-dimensional gradient phononic crystals *Appl. Phys. Lett.* **122** 112201
[33] Wang M *et al* 2018 Valley physics in non-hermitian artificial acoustic boron nitride *Phys. Rev. Lett.* **120** 246601
[34] Jiang H, Chen M, Liu Y, Yang T, Xu W, Liu Y, Zhang M and Wang Y 2019 Acoustic valley edge states in a graphene-like system with sub-wavelength resonator *J. Acoust. Soc. Am.* **146** 736–41
[35] Xi F, Tang Y and Hu L 2023 Valley edge states and chiral selective transport in reconfigurable phononic crystals *Eur. Phys. J.* B **96** 153
[36] Piñeiro M M, Plantier F, Bessières D, Legido J L and Daridon J L 2004 High-pressure speed of sound measurements in methyl nonafluorobutyl ether and ethyl nonafluorobutyl ether *Fluid Phase Equilib.* **222–223** 297–302
[37] Muhammad 2022 Phononic crystal based sensor to detect acoustic variations in methyl & ethyl nonafluorobutyl ether *Mater. Today Commun.* **32** 104127
[38] Lu J, Qiu C, Ye L, Fan X, Ke M, Zhang F and Liu Z 2017 Observation of topological valley transport of sound in sonic crystals *Nat. Phys.* **13** 369–74
[39] Mousavi S H, Khanikaev A B and Wang Z 2015 Topologically protected elastic waves in phononic metamaterials *Nat. Commun.* **6** 8682